land

MDPI

Article

Effects of Zn^{2+} on Limestone Weathering and Carbon Sink in the Chaotian River Basin, Guilin, China

Liang Li [1,2], Zhiwei Jiang [1,*], Bingjin Wu [1] and Wenhai Wang [1]

[1] College of Environmental Science and Engineering, Guilin University of Technology, Guilin 541006, China; liliangjiaxiang@163.com (L.L.); 2120200520@glut.edu.cn (B.W.); 2120210564@glut.edu.cn (W.W.)
[2] Guangxi-Key Laboratory of Theory and Technology for Environmental Pollution Control, Guilin University of Technology, Guilin 541006, China
* Correspondence: 2120220604@glut.edu.cn

Abstract: In this paper, the generation of inorganic carbon (mainly HCO_3^-) in a karst system (soil-limestone system) under karst soil and non-karst soil conditions was investigated using two Zn^{2+} concentrations and water flow rates. The results showed that (1) the dynamic equilibrium state of the chemical weathering of limestone is altered by Zn^{2+}, which is the primary cause of the change in HCO_3^- in soil-limestone systems; (2) ion exchange and adsorption are the primary characteristics of Zn^{2+} depletion under 1 mg/L $ZnCl_2$ settings, whereas Zn^{2+} under 50 mg/L $ZnCl_2$ conditions created two new solid phases ($Zn_5(OH)_6(CO_3)_2$, $ZnCO_3$) in the soil-limestone system; (3) the dissolution rate of limestone increases with the water flow rate, which facilitates the dissolution process; (4) the notable difference in ion release between non-karst and karst soil conditions could potentially be attributed to variations in the mineral composition, specific surface area, and particle size of the two soil types; (5) the combination of SEM, XPS, FT-IR, and XRD microstructure observation methods reveals that when limestone is exposed to a high flow rate (1.23 mL/min) and a high concentration (50 mg/L) of $ZnCl_2$, it experiences obvious dissolution and surface precipitation phenomena, as well as a significant change in HCO_3^- content.

Keywords: karst environment; Zn^{2+}; inorganic carbon; chemical weathering

Citation: Li, L.; Jiang, Z.; Wu, B.; Wang, W. Effects of Zn^{2+} on Limestone Weathering and Carbon Sink in the Chaotian River Basin, Guilin, China. *Land* **2024**, *13*, 1390. https://doi.org/10.3390/land13091390

Academic Editor: Yongheng Gao

Received: 24 June 2024
Revised: 23 August 2024
Accepted: 26 August 2024
Published: 29 August 2024

1. Introduction

The karst region of Southwest China has drawn attention to the issue of soil heavy metal pollution, which has been shown to impact soil biomass and physicochemical properties, as well as altering the natural ecological environment and human health through the enrichment effect [1–3]. A considerable amount of underground metal minerals were exposed to the surface due to the wide distribution of mineral resources that were mined and smelted, as well as other activities that resulted in soil heavy metals exceeding the standard. This increased element release into the environment led to soil heavy metal pollution [4]. It is indicated that the main cause of heavy metal contamination in the southwestern karst region is the geological high background due to the weathering of carbonate rocks into soils [5]. This weathering process also leads to significant leaching of Ca, Mg, and other soluble fractions from carbonate rocks, which leaves behind residual heavy metal elements (Zn, Mn, Cd, As, Pb, Hg, and so forth) in soils [6,7]. These elements are then transported through the environment by precipitation, adsorption, and complexation, and they are ultimately enriched and stabilized in the environment [8]. In addition, carbonate rocks actively participate in the global carbon cycle due to their ability to recycle atmospheric and soil CO_2 through chemical weathering to produce a carbon sink effect [9–11], and the carbon sink fluxes produced by their chemical weathering are 50.5% of those of terrestrial vegetation, 68% of those of forests, and 2.68 times those of scrubland, respectively [12]. Therefore, it is of vital significance to study the influence of the interaction between heavy metal ions and carbonate rocks on the effect of geological carbon sinks. The majority of

researchers focus on three areas of heavy metal pollution: toxicity, the ecological environment, and prevention and control. Xishen Zheng [13] and Aiping Zhu [14] provided an overview and analysis of heavy metal toxicology, as well as the route by which these metals enter the human body. Plant roots absorb heavy metals, which then make their way into the human body through the food chain and mix with bodily proteins to generate toxic conjugates that damage human cell membrane function and cause a host of poisoning symptoms that pose a threat to human health. Heavy metal pollution has become a significant factor affecting the safety of the ecological environment, as demonstrated by Jiaokun Li [15] and Juan Liu [16], who also showed how it destroys the normal material exchange and energy flow of the soil system, deteriorates soil quality, lowers crop yields, and affects soil microbial biomass, population size, community structure, and soil enzyme activity; The main countermeasures for prevention and control, both domestically and internationally, were outlined by Yue Hui [17] and Shibao Chen [18]. These included the need for the establishment of a scientifically standardized management system, increased data sharing about soil environmental monitoring, a decrease in the use of fertilizers and pesticides without scientific backing, the mitigation, reduction, and even prevention of heavy metal pollution its root causes, and the remediation of contaminated areas through the use of piles, chemical oxidation, electrodynamic separation, heat-treatment remediation techniques, topsoil, soil tillage, and soil replacement. Few scholars have conducted relevant studies in the field of the influence of the chemical weathering of carbonate rocks with the participation of heavy metal ions on the effect of geological carbon sinks.

The IPCC Fifth Assessment Report (Working Group I) identifies silicate weathering, carbonate weathering, and "rock weathering carbon sinks" as techniques for absorbing atmospheric CO_2 [19]. Qing Wu [20] noted that the carbon sinks created by weathering rocks, particularly carbonate weathering carbon sinks, play an active role in the global carbon cycle. Xiaoqun Qin [21] also demonstrated that carbonate rock weathering, or the production of carbon sinks by karst, is thought to represent a significant portion of lost carbon sinks by analyzing the rate at which rocks weather in the Pearl River Basin and estimating the carbon sinks. By examining the impact of Pb ions on the dissolution of dolomite, Tianyu Guan [22], was able to demonstrate that the active sites on the surface of the material were involved in the significant inhibition of Pb in the dissolution of dolomite, which changed the dissolution morphology, prevented the further development of the dissolution morphology, and inhibited the dissolution process for the surface of dolomite. Water samples from two surface river water locations in Shegongping Village were taken for examination and indoor simulation tests by Liang Li et al. [4,23] to show how lead ions influenced the process of geological carbon sinks and slowed the weathering of rocks under specific conditions. It is evident that there is a dearth of research on the impact of heavy metal elements on geological carbon sinks and the chemical weathering of carbonate rocks. More research is necessary to fully understand the connection between heavy metal elements and geological carbon sinks. Previous studies have demonstrated that the primary influencing elements in carbon sinks can be indirectly illustrated through the modeling of the interaction between Ca^{2+}, Mg^{2+}, and HCO_3^- [24]. The total quantity of HCO_3^- and other ions during the carbon cycle is probably impacted by Zn^{2+}, a common active heavy metal ion. As a result, for this study, we created indoor dynamic experiments with the heavy metal zinc (Zn) as the target element. We then used hydrochemical processes in conjunction with XRD, SEM, FT-IR, XPS, and other characterization techniques to analyze the relationship between Zn^{2+} and Ca^{2+}, Mg^{2+}, and HCO_3^- in the water-soil-rock system, as well as to investigate the mechanism of Zn^{2+}'s influence on the effects of geological carbon sinks.

2. Materials and Methods

2.1. Study Area

The study area is situated in Lingchuan County, Guangxi's Chaotian River basin (Figure 1). The landform's main body is a conventional peak cluster depression. The region

experiences 37 °C highs and −2 °C lows, with an annual average temperature of 17.5 °C and 285 days without frost. The research area has plentiful rainfall due to the effect of the warm and moist monsoon ocean. In total, 1601 mm of precipitation and 850.1 mm of land evaporation are experienced annually, on average [25]. Zinc is the target element in this study, which uses lead-zinc ore from Guilin City's Lingchuan County as its research object. The Zhuang Autonomous Region of Guangxi is home to the Lingchuan lead and zinc mine, which is situated on the Zuo River in Shigongping Village, Dajing Yao Township, Lingchuan County. About 200 mines were located in the mine region; mining is now closed, while illicit mining does occasionally take place (mostly during the dry season). There is a mine in the upper reaches of the Youjiang River in Shegongping, but it has not been mined. Since mining is underground, without refining, and there is no man-made destruction of vegetation, the cultivated land is in the lower part of the river, so there is no influence of other human activities except mining.

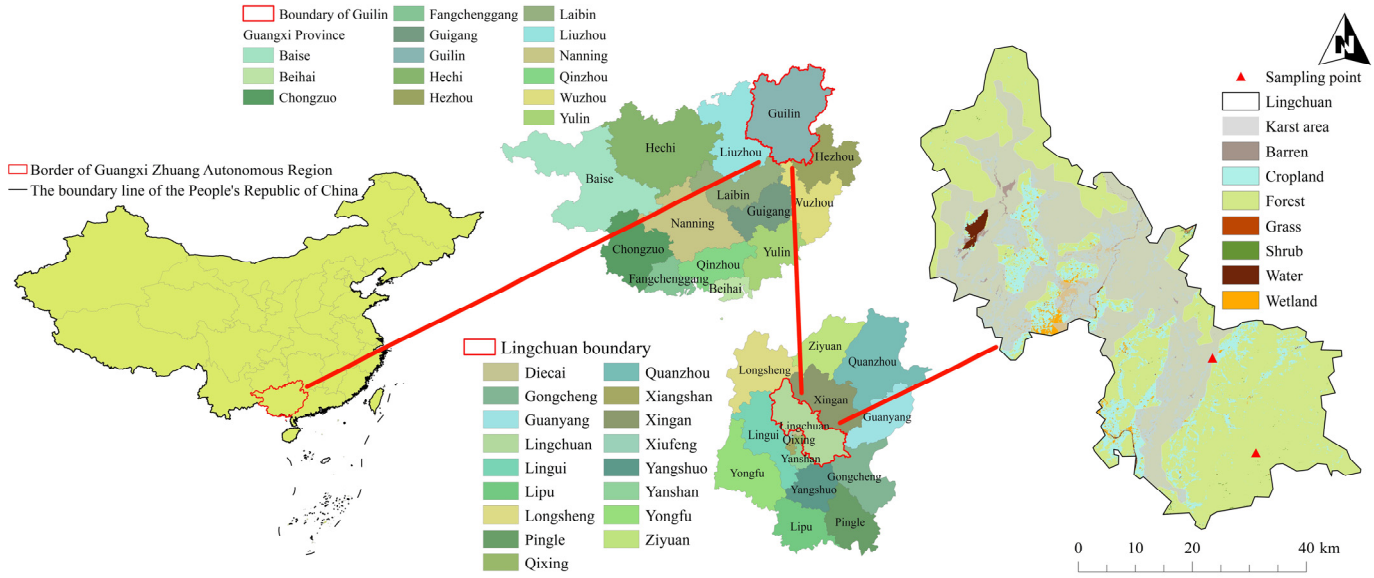

Figure 1. Location of the study area and sampling point.

The stratigraphic lithology in the study area, from old to new, is as follows: the lower Middle Devonian (D^1_2) is gray-gray, gray-green, and purplish red sandstone, siltstone, and shale. The upper middle Devonian Donggangling Formation (D_2d) is composed of iron-bearing argillaceous bioclastic limestone at the bottom, deep gray to gray-black barenaceous dolomite and gray dolomite sandwiched limestone in the middle and lower parts, and gray and dark gray limestone and an interlayer between limestone and dolomite at the upper part, with great variation in thickness. The upper part of the Rongxian Formation (D_3r) is a thick, light gray layer of limestone with an oolitic structure, and the lower part is a gray-black medium-thick layer of limestone. The lower part of the Liujiang Formation (D_3l) is mainly composed of siliceous rocks and siliceous shale, while the upper part is mainly composed of lenticular limestone and argillaceous limestone. The Lower Series C_1y is mainly composed of gray-black medium-thickness stratified limestone, dolomitic limestone, and dolomite, and partly contains argillaceous limestone and siliceous rock. Quaternary (Q), mainly clay, is mainly distributed on the northern border of the ocean valley, hoje, and scattered at the bottom of various depressions. The thickness is generally 5~10 m [26].

2.2. Materials and Preparation

The karst area of Saidi, Lingchuan County, Guilin City, and the non-karst area of Shegongping, Lingchuan County, Guilin City, provided the karst and non-karst soils, respectively, which were employed in the experiment. Samples were collected using the

mixed sample methodology, which guaranteed the representativeness of the samples. According to the diagonal sampling technique, the diagonal line in the sample region was divided into five equal portions, and each equal point was selected as the sampling point. A collection of 0–10, 10–20, and 20–30 cm of surface soil was made. The soil was then mixed uniformly and left in the laboratory to dry naturally. Processing was carried out with the specifications of the Land Quality Geochemical Evaluation" (DZ/T 0295-2016) standard [27]. Table 1 displays the physicochemical parameters of the soils. The X-ray diffractometer identified the mineral composition of the limestone samples, which were obtained in Shegongping, Lingchuan County, Guilin City, as $CaCO_3$ and a trace amount of SiO_2 (Figure 2). The collected soil and limestone samples were naturally air-dried in the chamber, and the large stones and plant residuesin the soil samples were removed before being ground with ceramic mortar and screened through 100 mesh (0.149 mm). The samples were acquired using the quarter method. The residual soil samples were filtered with 20 mesh (2 mm) and put in plastic bags for sealing and preservation. Before being loaded into the experimental column, limestone was broken up with a hammer and ground into 1–3 mm particles using a ceramic mortar. Superior pure $ZnCl_2$, which was obtained from Xilong Science Co., Shantou, China. and diluted with ultrapure water to the appropriate concentration before the experiment, was the experimental reagent employed in the study. Before being dried under 50°C in an electric blast drying oven and stored for later use, the high-purity quartz sand used in the laboratory was washed of surface impurities using tap water, and then soaked in and cleaned with ultrapure water.

Table 1. Results of physicochemical property measurements of soil.

Project Name	Karst Soil	Non-Karst Soils
PH	6.77	4.37
proportion	2.54	2.65
Capacity ($g \cdot cm^3$)	1.20	1.17
Ca ($mg \cdot g^{-1}$)	5540.17	4320.56
Mg ($mg \cdot g^{-1}$)	259.30	20.00
Zn ($mg \cdot g^{-1}$)	31.16	77.66
Pb ($mg \cdot g^{-1}$)	121.91	77.66

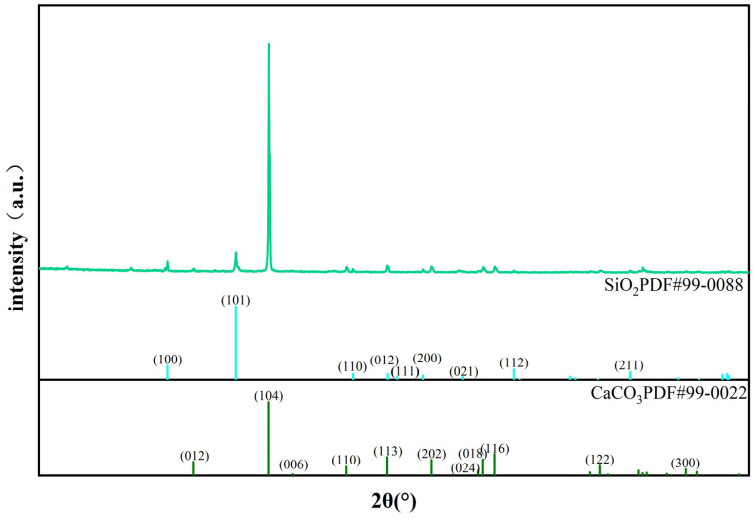

Figure 2. XRD diffractogram of the test limestone.

Using a pH meter, pipette method, or ring knife method, respectively, one may test the pH, specific gravity, and bulk density of soil. After microwave digestion, two milliliters of nitric acid and one milliliter of hydrofluoric acid were added, the digestion tank was rinsed with 0.2% nitric acid solution, and the volume of ultra-pure water was fixed to the scale line. The contents of Ca, Mg, Zn, and Pb were then measured using an

inductively coupled plasma emission spectrometer (ICP-OES, PerkinElmer, Waltham, MA, USA, Optima 7000DV).

2.3. Methods of Characterization and Analysis of Limestone and Soil

The morphology of limestone and soil was analyzed by SEM (GeminiSEM 300, Zeiss, Jena, Germany). The dried minerals were fully ground with an agate mortar, and a small amount of powder was evenly dispersed on the loading table with conductive tape. The floating powder on the surface of the sample was purged by a blower, and a film was applied to the sample for 30 s of vacuum gold spraying to increase its conductivity. The sample was placed in the electron microscope observation chamber, the voltage was set, the brightness and magnification were adjusted appropriately, and then the focus mode was automatically focused, the dissipated image was eliminated, and the fast scan or slow scan mode was pressed to obtain a clear image and save it [28]. The mineral composition of the material was measured by XRD (PANalytical B.V., NED, X, Pert3Power, Eindhoven, The Netherlands), which mainly analyzed the crystallization type, material composition, and internal structure of the adsorbed material. The instrument parameters were as follows: Cu Ka target (45 kV, 40 mA), scanning speed 10°/min, and scanning angle 10~90°, respectively [29]. The XRD patterns were analyzed by MDI JADE 6.5 software and Origin 2022. FT-IR (Thermo Fisher, Waltham, MA, USA, Nicolet™) was used to analyze the chemical bonds inside the structure of the dry materials. The dried minerals or samples were passed through a 200-mesh screen, and the spectral pure KBr was used as the infrared absorption background [30]. The samples and KBr were fully ground in an agate mortar at a ratio of 1:100 to ensure the two were mixed evenly. A certain amount of the mixture was placed in the pressing mold, placed in the tablet press at a pressure of 15 MP for 20~30 s to form a film, and lastly it was scanned using a 4000~400 cm^{-1} scanning range to gather infrared spectra. XPS (Thermo Fisher, Waltham, MA, USA, K-Alpha) uses X-ray radiation samples to stimulate the inner-layer electrons or valence electrons of atoms or molecules to be emitted, and measures the emitted photoelectron energy to obtain the elemental changes and chemical bond binding energy changes in samples [31].

2.4. Experimental Setup and Methods

The experiment was a dynamic adsorption study consisting of three sets of tests with varying Zn^{2+} concentrations (group I), flow rates (group II), and soil conditions (group III) while maintaining constant external conditions. Table 2 displays the experimental group names and conditions.

Table 2. Experimental group names and conditions.

Group Name	Experimental Conditions
Group I	Zn^{2+} concentrations of 0, 1, and 50 mg/L, flow rate of 0.41 mL/min, and karst soil conditions
Group II	Zn^{2+} concentrations of 0, 1, and 50 mg/L, flow rate of 1.23 mL/min, and karst soil conditions
Group III	Zn^{2+} concentrations of 0, 1, and 50 mg/L, flow rate of 1.23 mL/min, and non-karst soil conditions

Figure 3 displays the schematic diagram of the experimental setup. An acrylic column, 25 cm in height and with an inner diameter of 5 cm, was used for the experiment. The column was filled with circular qualitative filter paper, 2.5 cm of quartz sand, 5 cm of limestone, 15 cm of test soil, and 2.5 cm of quartz sand from bottom to top before the experiment. Quartz sand was added to ensure that the inflow solution could pass through the material in the column uniformly [32]. The column was then connected to a peristaltic pump and exposed to three different concentrations of $ZnCl_2$ (0, 1, and 50 mg/L) by pumping the solution upward. Periodic samples were taken from the column effluent and

analyzed for HCO_3^- content using a titration kit with an accuracy of 0.1 mmol/L. The samples were then filtered through a nylon microporous membrane with a pore size of 0.45 µm and analyzed using ICP-OES, (PerkinElmer, Waltham, MA, USA, Optima 7000DV) to measure changes in Zn^{2+}, Ca^{2+}, and Mg^{2+} concentrations under altered conditions. Experiments were conducted to characterize soil and limestone and to analyze surface dissolution and crystal attachment.

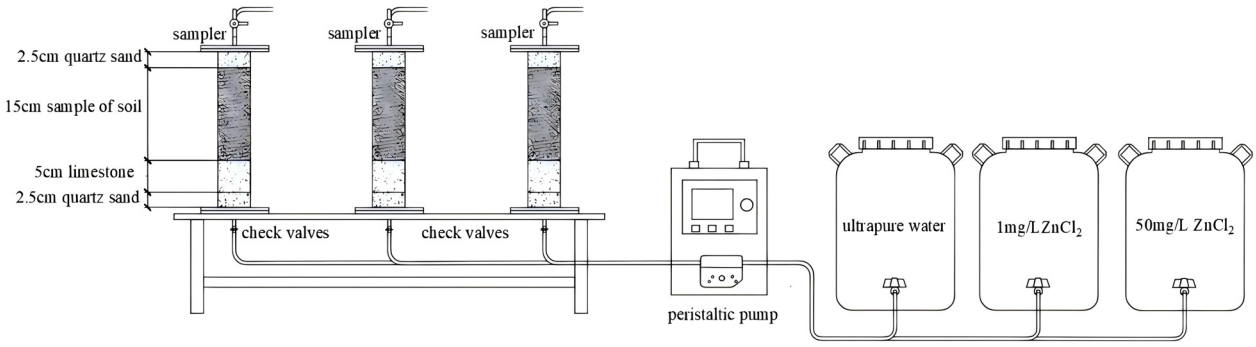

Figure 3. Schematic diagram of the experimental setup.

3. Results and Discussion

Curves of the Ca^{2+}, Mg^{2+}, Zn^{2+}, and HCO_3^- concentrations were drawn to investigate the impacts of changes in heavy metal ions and inorganic carbon contents in soil-limestone systems with various Zn^{2+} concentrations, flow rates, and soil types (Figures 4–6).

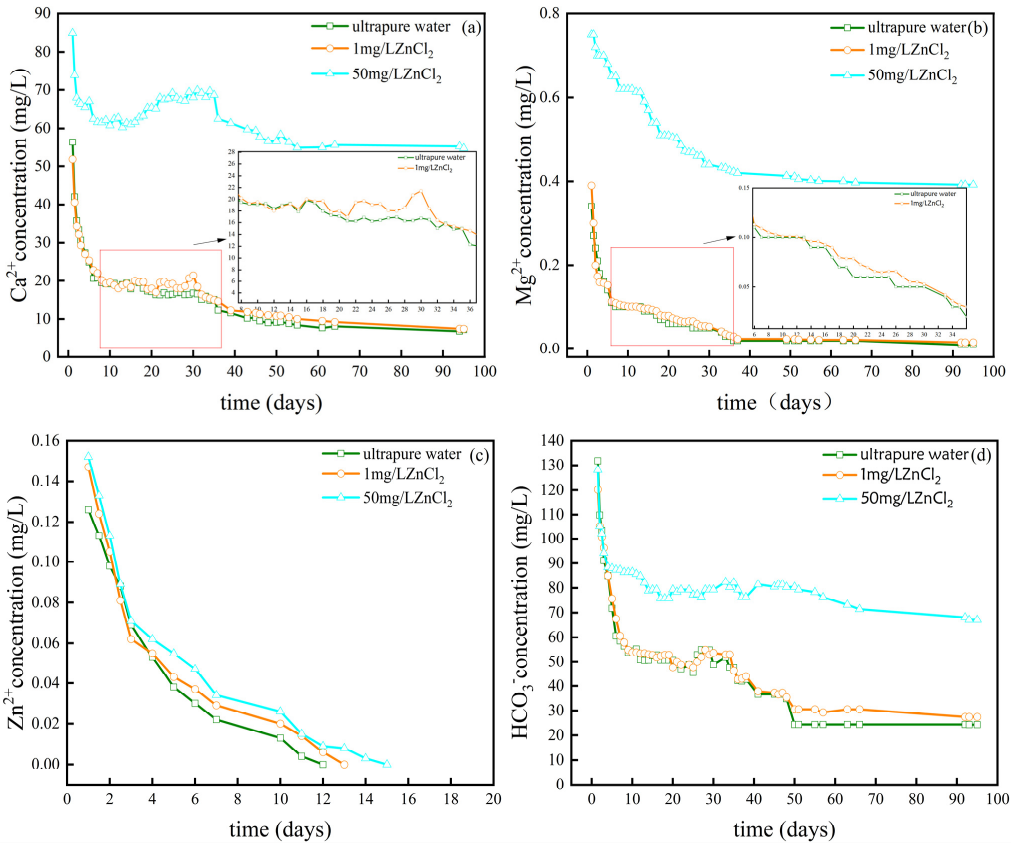

Figure 4. The concentration changes of ions with different concentrations of Zn^{2+}: (**a**) Ca^{2+}; (**b**) Mg^{2+}; (**c**) Zn^{2+}; (**d**) HCO_3^-.

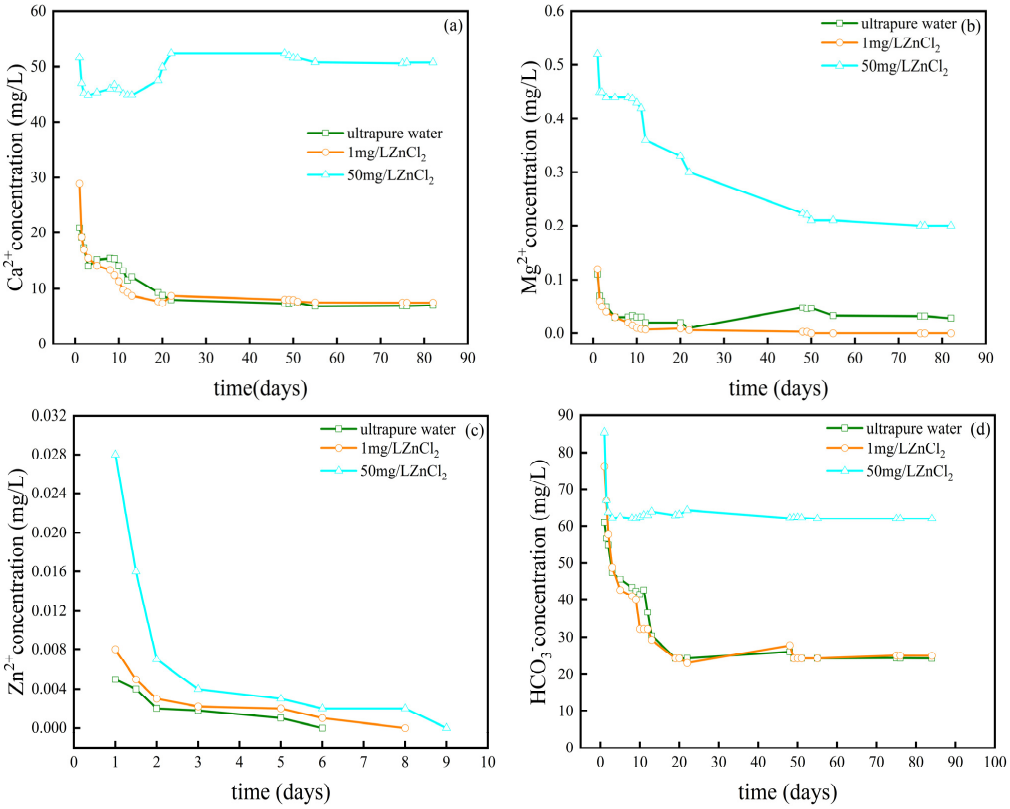

Figure 5. The change in ion concentration with the flow rate of aqueous solution (1.23 mL/min): (**a**) Ca^{2+}; (**b**) Mg^{2+}; (**c**) Zn^{2+}; (**d**) HCO_3^-.

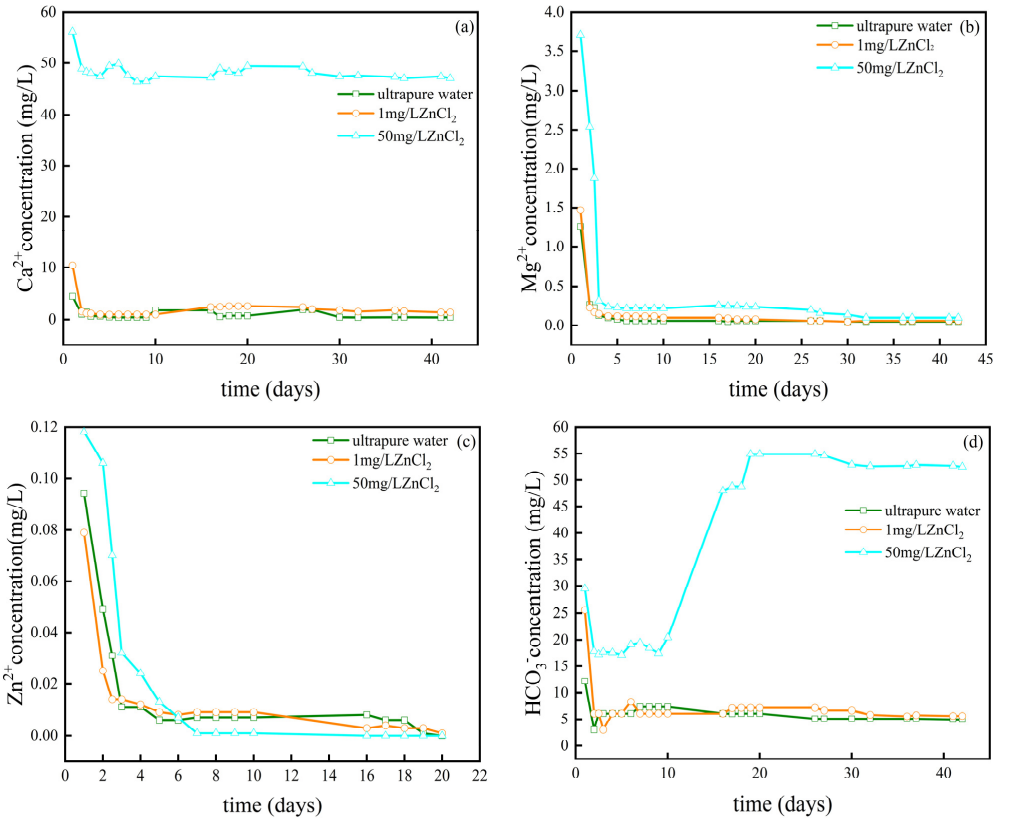

Figure 6. The changes in ion concentration under the non-karst soil conditions: (**a**) Ca^{2+}; (**b**) Mg^{2+}; (**c**) Zn^{2+}; (**d**) HCO_3^-.

3.1. Hydrochemical Processes in Soil-Limestone Systems

3.1.1. Analysis of Changes in the Concentration of Each Metal Ion and Inorganic Carbon Based on Different Zn^{2+} Concentrations

The changes in the Ca^{2+} concentration during the reaction involving various Zn^{2+} solution concentrations typically displayed a downward trend, indicating a negative correlation (Figure 4a). When 50 mg/L $Zncl_2$ solution was added to the soil-limestone system, the Ca^{2+} concentration consistently outperformed the other two Zn^{2+} concentrations. The experimental columns subjected to 1 mg/L and 50 mg/L Zn^{2+} also showed a slow-rising phase in the Ca^{2+} concentration over a period of 10 to 30 days. This phenomenon can be explained by the fact that, at this point, the limestone surface $Zn_5(OH)_6(CO_3)_2$ and a small amount of $ZnCO_3$ growth consumed the $CO_3{}^{2-}$ in the water column, weakening the $CO_3{}^{2-}$ hydrolysis effect and intensifying the $CaCO_3$ dissolution [33]. When the Ca^{2+} concentration was stable until day 95 of the experiment, the experimental column Ca^{2+} concentration of 50.13 mg/L under the influence of 50 mg/L of $ZnCl_2$ was still much higher than those of the 7.98 mg/L under 1 mg/L and 7.74 mg/L under ultra-pure water. The main equations involved in this process are as follows [34]:

$$CaCO_3 \Leftrightarrow Ca^{2+} + CO_3^{2-} \quad (1)$$

$$CO_3^{2-} + H_2O \Leftrightarrow HCO_3^- + OH^- \quad (2)$$

$$Zn^{2+} + CO_3^{2-} = ZnCO_3 \quad (3)$$

$$5Zn^{2+} + 6OH^- + 2CO_3^{2-} = Zn_5(OH)_6[CO_3]_2 \quad (4)$$

The concentration of Mg^{2+} in the liquid sample is shown in Figure 4b, trajectory to that of Ca^{2+}, decreasing with time until it stabilized within a narrow range. Compared to the Ca^{2+}, the Mg^{2+} content was substantially less than 1 mg/L at the initial concentration. The explanation for this is that the dissolution-precipitation interaction of the limestone with the Zn^{2+} produced the Ca^{2+} found in the liquid samples. The X-ray mineral diffraction (XRD) revealed that the sample's primary mineral components were $CaCO_3$ and a trace quantity of SiO_2. No Mg-containing inorganic compounds were found, indicating that the Mg^{2+} likely originated from the cation exchange between the Zn^{2+} and the karst soil. The Mg^{2+} content reached a peak of 0.75 mg/L on the first day of the 50 mg/L experimental column and dropped to a low of 0.1 mg/L on the 92nd day of the ultra-pure water experimental column [35]. Prior studies have demonstrated that bivalent Zn, Cd, Ni, Mn, and other cations exhibit high adsorption onto the surface of calcium carbonate [36]. The Zn^{2+} was adsorbed and rapidly decreased in the soil-limestone system, as shown in Figure 4c. The coarse texture of limestone offers stable contact and serves as an adsorption site for Zn^{2+} [37,38]. Chemisorption takes place when a 1 mg/L $ZnCl_2$ solution interacts with a karst-soil-limestone system, whereas at a higher concentration of 50 mg/L $ZnCl_2$ solution, metal ions mostly adhere to carbonate minerals via cation exchange and precipitation. When Zn^{2+} reacts with $CO_3{}^{2-}$ and OH^-, it forms $Zn_5(OH)_6(CO_3)_2$ (hydrozinkite) and a small quantity of $ZnCO_3$ on the mineral's surface [33]. The concentration of Zn^{2+} in each experimental column decreased to 0 on the 12th, 13th, and 15th days, respectively. In Figure 4d, the concentration of $HCO_3{}^-$ fell considerably within 1–10 days under the influence of varying Zn^{2+} concentrations, followed by a gradual fall stage. The concentration of $HCO_3{}^-$ reached a steady level on the 63rd day of the experiment. $HCO_3{}^-$ content in the outflow liquid of the ultra-pure water, 1 mg/L $ZnCl_2$, and 50 mg/L $ZnCl_2$ test columns were measured at 24.41 mg/L, 30.51 mg/L, and 73.22 mg/L, respectively. Both low and high concentrations of the Zn solution promoted the dissolving of the limestone, with a more pronounced effect observed at higher concentrations.

3.1.2. Analysis of Changes in the Concentration of Each Metal Ion and Inorganic Carbon Based on the Flow Rate of Aqueous Solution (1.23 mL/min)

Figure 5a–d illustrates how the Ca^{2+} concentration changed under high flow rate (1.23 mL/min) conditions and followed the same trend in less time than at low concentration. The concentration changes of the other ions also showed a negative time correlation with the changes in the Ca^{2+} concentration, and the concentrations of Mg^{2+}, Zn^{2+}, and HCO_3^- changed quickly, reaching a rapid equilibrium state after the decreasing phase. The state was caused by the fact that, during the dynamic dissolution of limestone, the mass transfer of reactants and products is facilitated by the local fluid velocity close to the mineral surface, and the dissolution rate is proportionate to the fluid flow rate, which increases with increasing fluid velocity [39,40]. Furthermore, mechanical damage to the surfaces of rock samples might result from the erosive effect of water flow on soil-limestone systems [41,42]. This damage can be readily seen in the following characterization observation methods, including XRD and SEM. When the experiment progressed to the 2nd, 3rd, and 4th days, the Zn^{2+} concentration hardly changed, and the Zn^{2+} concentrations in the experimental columns were 0.002 mg/L, 0.002 mg/L, and 0.003 mg/L, respectively. The flow rate had less of an impact on the change in Mg^{2+} concentration, and it took about the same amount of time to bring the reaction to equilibrium as it did at low flow rates. Overall, under high flow rate reaction conditions, the ionic reaction reached the equilibrium state 1.12–1.63 times faster than under low flow rate conditions. At the beginning of the reaction, the limestone (the main component of $CaCO_3$) rapidly dissolved in the water, the water-rock reaction was intense, and the concentrations of Ca^{2+} and HCO_3^- were larger compared with those of the other metal ions. However, as the experiment proceeded, the Ca^{2+}, Mg^{2+}, Zn^{2+}, and HCO_3^- underwent homoiconic effects, the water-rock effect thus gradually weakened, and the concentration of each ion in the karst-soil-limestone system reached equilibrium at concentrations lower than those in the conditions of the lower flow rates. These results are similar to those in a study conducted by Shi Xufei et al. [43].

3.1.3. Analysis of Changes in the Concentration of Each Metal Ion and Inorganic Carbon Based on Non-Karst Soil Conditions

When the soil condition was non-karstic, the non-karstic soil-limestone system reached a reaction equilibrium faster than the karstic soil-limestone system (Figure 6a). The concentrations of Ca^{2+}, Mg^{2+}, and Zn^{2+} in the soil-limestone system were all negatively correlated with time. While the ion concentration in the karst soils declined significantly in the first 20 days, the decrease in the Ca^{2+} concentration in the non-karst soil conditions was more visible on days 1–8. The Mg^{2+} concentration changes under non-karst soil conditions are depicted in Figure 6b, following the same pattern as in the karst soil conditions, where the Mg^{2+} concentration reached a relatively stable state following a brief period of rapid decline. Under non-karst soil conditions, the Zn^{2+} decreased quickly with an increase in reaction time. When the reaction reached an equilibrium, Zn^{2+} was not detectable in the 50 mg/L $ZnCl_2$ group; at this point, the size relationship of the Zn^{2+} concentration was ultrapure water group > 1 mg/L $ZnCl_2$ group > 50 mg/L $ZnCl_2$ group (Figure 6c). The content of HCO_3^- in the non-karst soil experimental columns appears in Figure 6d. The three experimental columns show varying increases in HCO_3^- concentration from the fifth to the twentieth day. The phenomenon of rising concentration and the karst soil conditions at the time of the difference was not significant, in contrast to the other two concentrations of Zn^{2+} conditions, where the increasing trend of HCO_3^- content was more evident in the 50 mg/L $ZnCl_2$ solution. This effect was caused by an increase in the breakdown of $CaCO_3$ in the soil-limestone system as a result of the Zn^{2+} depleting the CO_3^{2-} in the solution [23]. There were notable variations in the release of ions (Ca^{2+}, Mg^{2+}, Zn^{2+}, and HCO_3^-) under various soil conditions. These variations were ascribed to the variations in the mineral composition, particle size, and specific surface area between the karst and non-karst soils, since a larger specific surface area can provide more adsorption sites [44]. The specific surface area of the non-karst soils was less than that of the limestone, Zn^{2+}

was more readily adsorbed on the limestone. In addition to the surface dissolution of limestone, the amount of HCO_3^- in soil-limestone systems is also influenced by the organic carbon in the soil breaking down to produce CO_2, which is dissolved in water and reacts to produce H_2CO_3. This process erodes limestone and modifies the HCO_3^- content of the soil-limestone system, which, in turn, affects the geological carbon sink [45,46].

3.2. Soil and Limestone Morphological Characteristics

3.2.1. XRD Analysis of Soil

The initial samples of karst and non-karst soils were analyzed using X-ray diffraction (XRD) to determine the nature of the soil surface deposits. The results are displayed in Figure 7, where the X-ray diffraction patterns of both soils are dominated by strong peaks of SiO_2, while the diffraction peaks of the $CaCO_3$ are relatively weak.

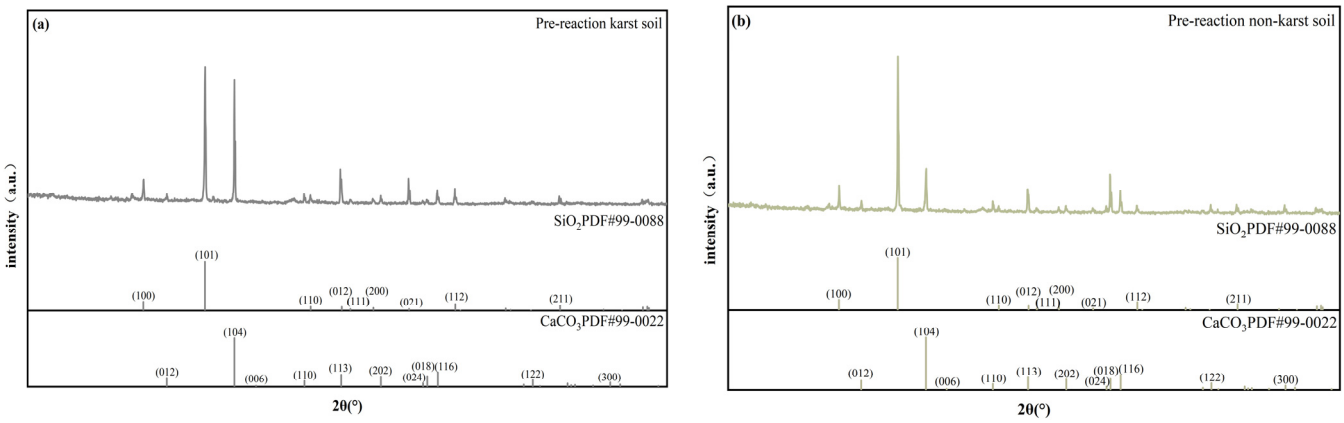

Figure 7. X-ray diffraction patterns of initial samples of soil: (**a**) karst soil; (**b**) non-karst soil.

Figure 8 shows the X-ray diffraction patterns of the two soils under different experimental conditions. When compared to the PDF card of the $CaCO_3$ (#99-0022), the XRD data for the three experimental groups (a: karst soil-low flow rate), (b: karst soil-high flow rate), and (c: non-karst soil-high flow rate) demonstrate that the composition of the solid-phase diffraction peaks was still dominated by strong peaks of SiO_2. Following the experiment, the two soils' $CaCO_3$ diffraction peaks were significantly reduced. The soils exposed to high concentration and high flow rate conditions, on the other hand, showed relatively weak $CaCO_3$ diffraction peaks compared to the two soils under the other conditions. Figure 8c provides a clearer view of the changes in $CaCO_3$ peaks under non-karst soil conditions. Furthermore, the diffraction peaks of the $CaCO_3$ at 2θ are situated at 13.066° (200), 28.401° (020), 30.591° (311), 36.190° (510), 43.340° (510), and 54.301° (800). These strong peaks are consistent with the standard positions of the $Zn_5(OH)_6(CO_3)_2$ and $ZnCO_3$ peaks. In the high concentration, high flow rate conditions of the two soils corresponding to the peaks in the XRD image, as opposed to in the low concentration, the low flow rates are relatively high. This time, the strong peaks correspond to the standard diffraction peak cards for $Zn_5(OH)_6(CO_3)_2$, PDF#19-1458, and for $ZnCO_3$, PDF#99-0095 [47,48].

Based on an analysis of the aforementioned phenomena, the Zn^{2+} was absorbed by the soil surface in large quantities in all three groups of experiments, with varying concentrations of $ZnCl_2$ solution. The concentration of Zn^{2+} in the solution rapidly decreased as it reacted with CO_3^{2-} and OH^- to create zinc hydrazine ore and zinc carbonate precipitate, which adhered to the soil surface [33]. The cation exchange between Zn^{2+} and soil, as well as soil erosion from water flow, could be the cause of the decrease in the peak value of the $CaCO_3$ diffraction peak on the soil surface. This erosion releases Ca^{2+}, which then contributes to the Ca^{2+} dynamic equilibrium within the limestone-and-soil system, along with Ca^{2+} from limestone. The Ca^{2+} concentration rising phase in the hydrochemical analysis might also have been caused by this Ca^{2+} phenomenon.

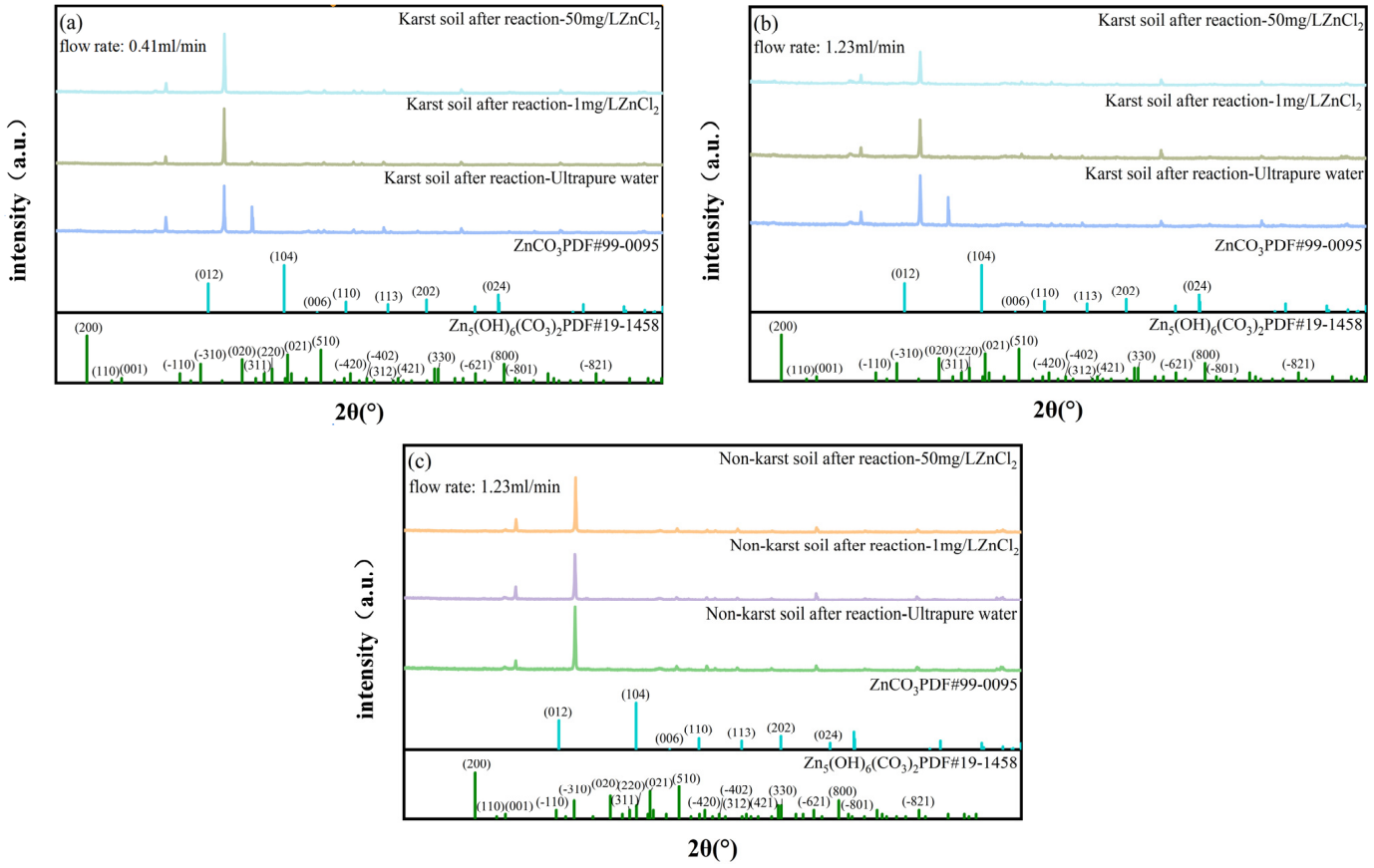

Figure 8. X-ray diffraction patterns of soils: (**a**) Group I, karst soils, 0.41 mL/min; (**b**) Group II, karst soils, 1.23 mL/min; (**c**) Group III, karst soils, 1.23 mL/min.

3.2.2. XRD Analysis of Limestone

Figure 9 displays the X-ray diffraction patterns of the limestone under several experimental conditions: low flow rate (for karst soil), high flow rate (for karst soil), and high flow rate (for non-karst soil). It is clear from the three experimental setups that $CaCO_3$ continued to dominate the strong peak composition of limestone, and there was little change in the general distribution features of the diffraction peaks. However, the diffraction peak of $CaCO_3$ in the limestone shows a more obvious downward trend at 1 mg/L and 50 mg/L $ZnCl_2$ (Figure 9a). At 1.23 mL/min, the diffraction peak strength of $CaCO_3$ in limestone drops significantly as the Zn^{2+} concentration increases (Figure 9b,c). This phenomenon can also play a significant role in the Ca^{2+} rising stage of hydrochemistry. It also confirms that, in the presence of high flow velocity, the erosion effect of water flow on the soil-limestone system promotes the decomposition of $CaCO_3$. In non-karst soil, the peak value of $CaCO_3$ in limestone with 1 mg/L and 50 mg/L $ZnCl_2$ involvement is larger than that in karst soil. This phenomenon's occurrence confirms the hydrochemical analysis's conclusions about the impact of limestone's specific surface area and non-karst soil on Zn^{2+} adsorption capability. Furthermore, the XRD pattern of the limestone indicates high peaks in the positions of the $Zn_5(OH)_6(CO_3)_2$ and $ZnCO_3$ peaks, with an intensity trend comparable to that of the soil. These findings support the formation of two distinct types of precipitates on the surfaces of the soil and limestone in the soil-limestone system.

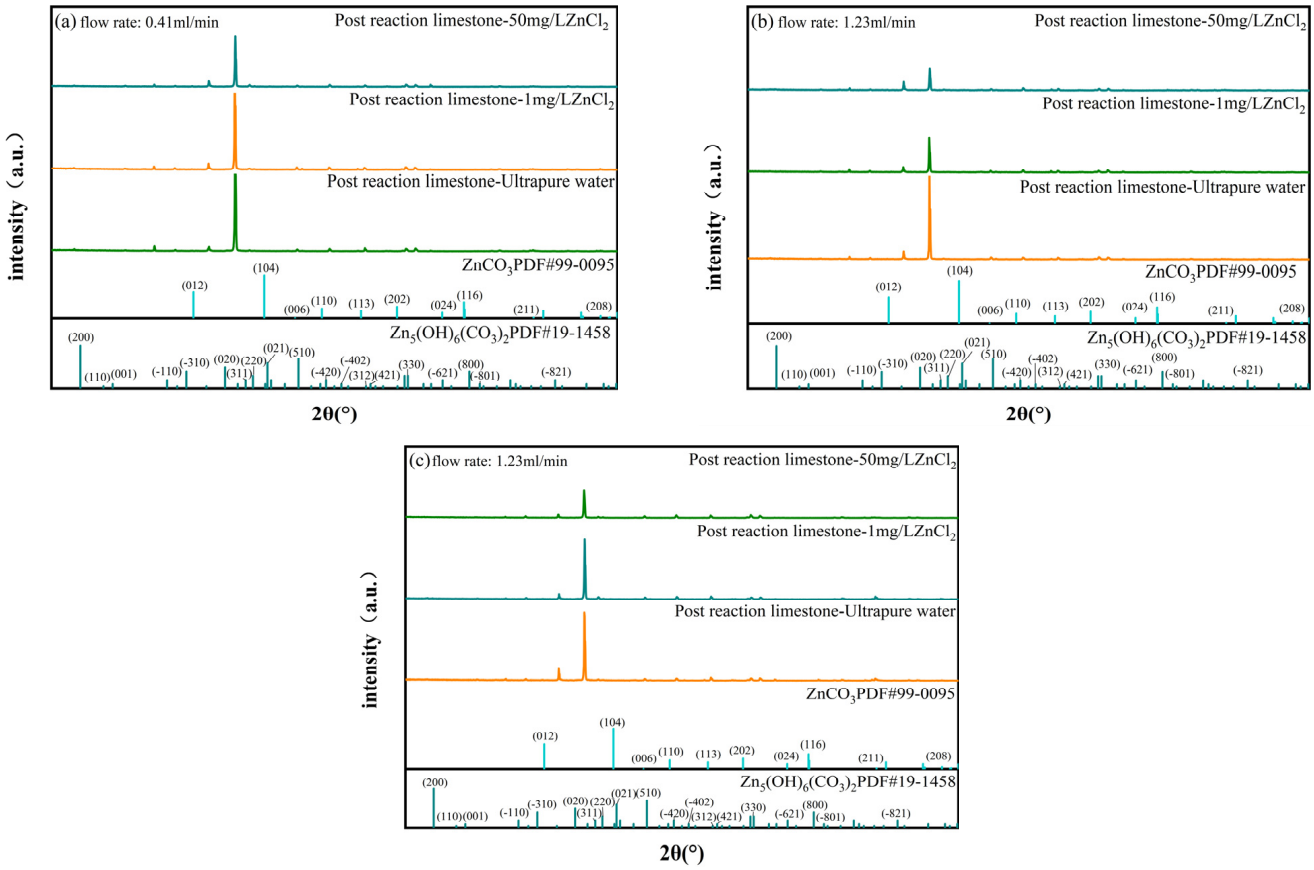

Figure 9. X-ray diffraction patterns of limestone: (**a**) Group I, karst soils, 0.41 mL/min; (**b**) Group II, karst soils, 1.23 mL/min; (**c**) Group III, karst soils, 1.23 mL/min.

3.3. FT-IR Mapping Analysis of Soil and Limestone

3.3.1. FT-IR Mapping Analysis of Soil

An experiment was carried out by FT-IR to observe whether the surface functional groups of the soil changed before and after the reaction in different environments, and the results are shown in Figure 10, which shows that the surface hydroxyl (-OH) telescopic vibration peaked near 3622 cm^{-1} in the karst soil before and after the reaction [49]. The bending vibration absorption peaks at 1636 cm^{-1} were attributed to the bending vibration of water [50], while the absorption peaks at 1425 cm^{-1} were attributed to the telescoping vibration of C=O in the karst soil prior to the reaction [51]. The absorption peak at 1025 cm^{-1} and 1019 cm^{-1} in non-karst soil was attributed to Si-O stretching vibration, while the two peaks near about 796 cm^{-1} were distinctive peaks of quartz [52]. The two peaks near about 693 cm^{-1} were created by the Si-O stretching vibration. When the soil condition was non-karst soil, the corresponding peaks at 3622 cm^{-1} in the figure were still hydroxyl group stretching vibration peaks; the peak at about 784 cm^{-1} was associated with the symmetric Si-O-Si stretching vibration; and the peak near about 692 cm^{-1} was caused by additional distinct quartz absorption peaks associated with the symmetric bending vibration of [SiO_4] tetrahedra [50]. In the FT-IR spectra of the soils before and after the adsorption process, differences in bonding between the metal ions at the active sites and the soil surface caused some of the functional group bands to shift, and it was found that no new functional groups were activated under the various environmental conditions.

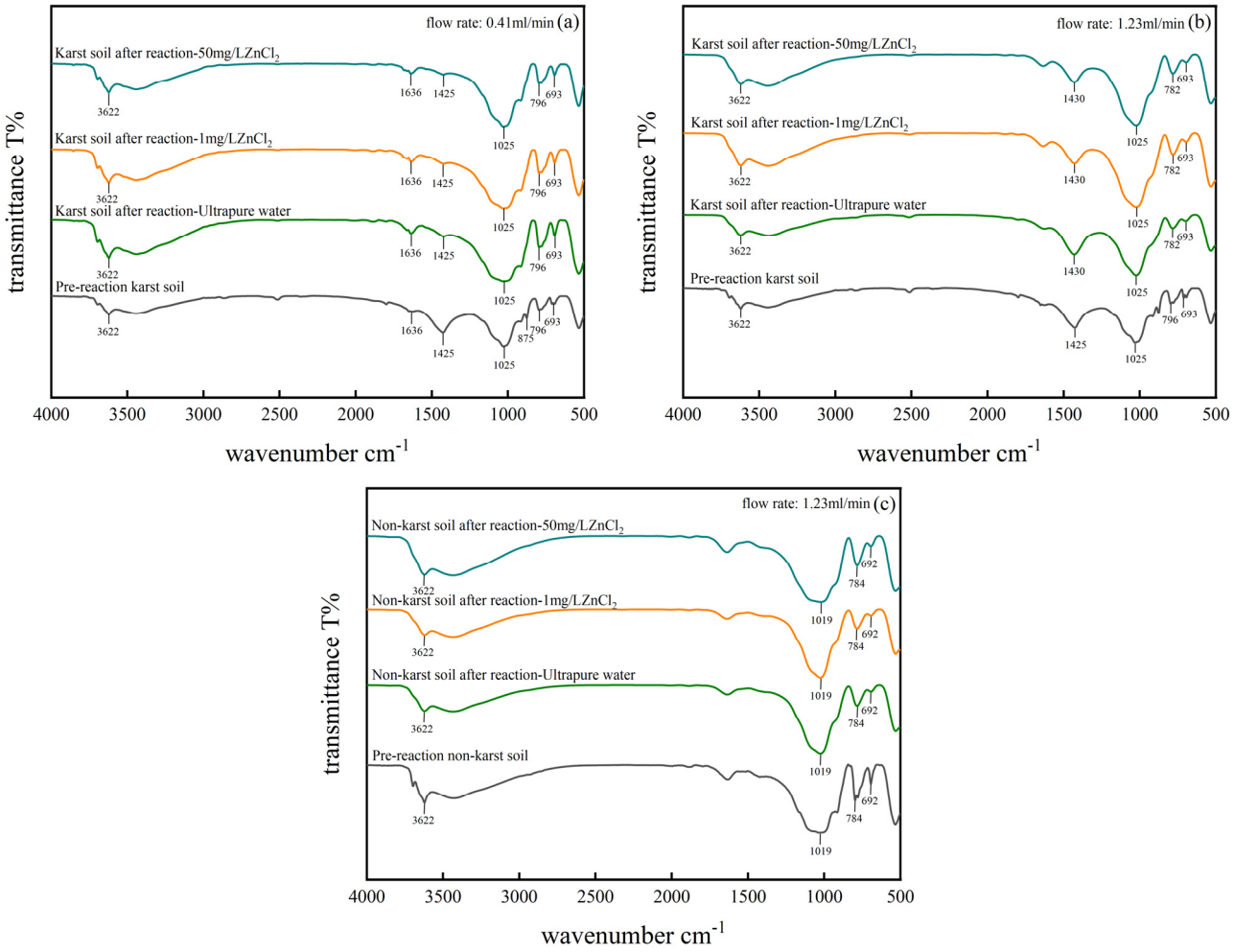

Figure 10. FT-IR profiles of soil: (**a**) Group I, karst soils, 0.41 mL/min; (**b**) Group II, karst soils, 1.23 mL/min; (**c**) Group III, karst soils, 1.23 mL/min.

3.3.2. FT-IR Mapping Analysis of Limestone

Figure 11 depicts the FT-IR spectrum of the limestone. When the soil condition was karst soil, the -OH bending vibration peak and telescopic vibration of the adsorbed water, 3621 cm^{-1} and 2513 cm^{-1}, respectively (Figure 11a,b) were also present on the surface of the limestone; 1799 cm^{-1} is the C=O telescopic vibration vibrational absorption peak [53]. The absorption peaks at 1427 cm^{-1}, 1428 cm^{-1}, 874 cm^{-1}, and 711 cm^{-1} are the absorption peaks of carbonate in carbonate minerals, among which the absorption peaks at 1427 cm^{-1} and 1428 cm^{-1} are the characteristic absorption peaks of calcite [54], which are caused by the asymmetric telescopic vibration of carbonate, the absorption peaks at 874 cm^{-1} are related to the out-of-plane bending vibration of the C-O bond, and the absorption peaks at 711 cm^{-1} are the in-plane bending vibration of C-O bonds.

The vibration absorption peak of the C=O stretching vibration at the initial 1799 cm^{-1} before and after the reaction was weaker when the soil condition was non-karst (Figure 11c). The absorption peaks of three different wave numbers of carbonate near 1427 cm^{-1} were mostly found on the limestone surface as a result of the interaction between the Zn^{2+} and the CO_3^{2-}. To some extent, CO_3^{2-} is consumed in this process, and the area of the peaks and peak value are weakened [55].

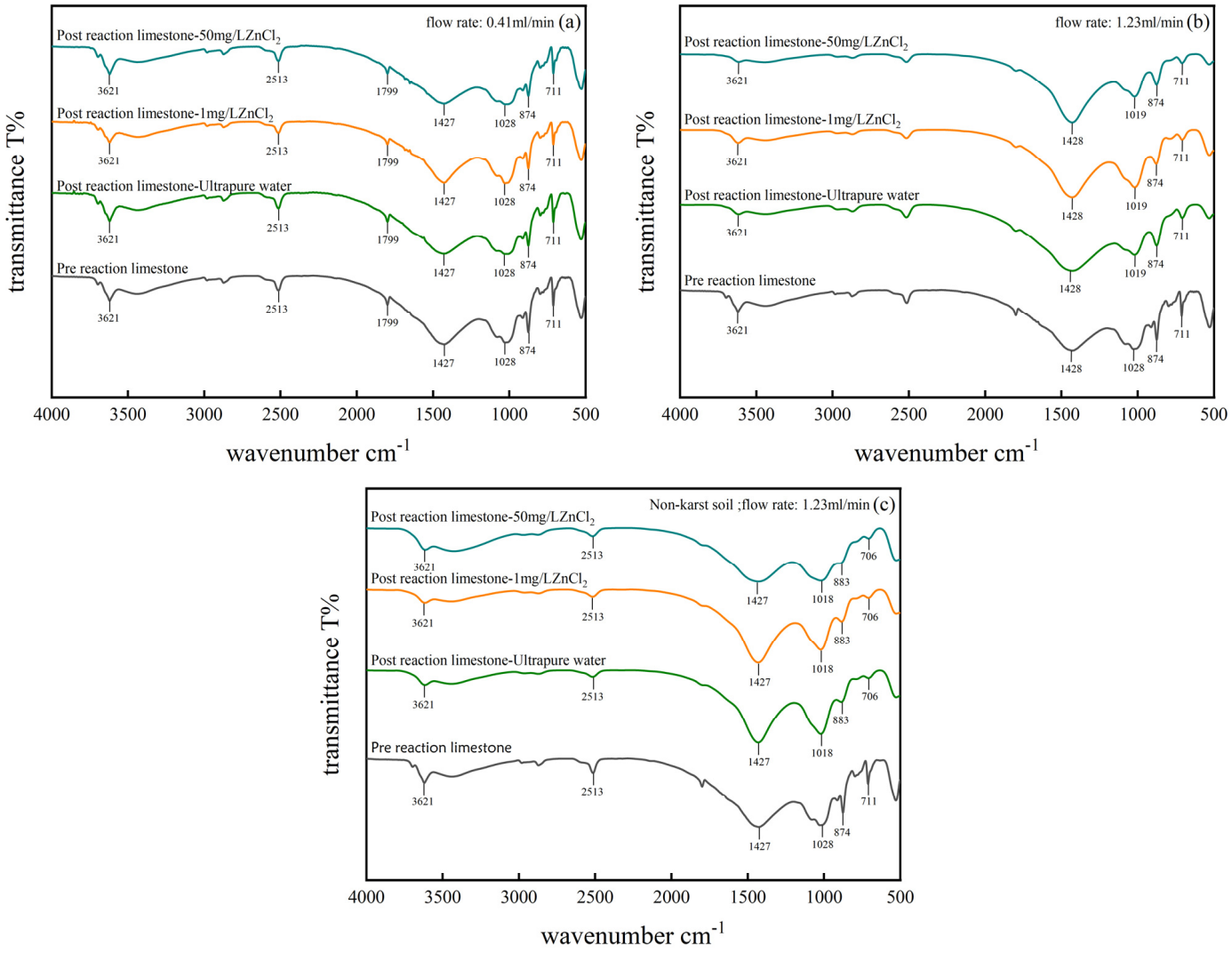

Figure 11. FT-IR profiles of limestone: (**a**) Group I, karst soils, 0.41 mL/min; (**b**) Group II, karst soils, 1.23 mL/min; (**c**) Group III, karst soils, 1.23 mL/min.

3.4. SEM Mapping Analysis of Soil and Limestone

3.4.1. Soil Morphological Characteristics

Figure 12a,d depicts SEM images of the karst soil morphology under different reaction circumstances. Prior to the reaction, the karst soil's surface was made up of multilayered lamellar platelets. Following the interaction with the ultrapure water, 1 mg/L $ZnCl_2$, and 50 mg/L $ZnCl_2$, the specific surface area of the karst soil decreased, and the number of platelets decreased more dramatically as the concentration of Zn^{2+} increased. This is assumed to have been the result of the karst soil and solution coming into contact, resulting in a cationic exchange of Ca^{2+} and Zn^{2+} in the pore space and thinning of the soil particles' hydration film. This caused the soil particles to come together, resulting in the development of aggregates and agglomerates, reducing the karst soil's specific surface area [56].

Figure 12e–g shows the shape of the karst soil before and after the response at different flow rates. The flow rate rose from 0.41 mL/min to 1.23 mL/min and the karst soil's general shape altered slightly. The high concentration of Zn^{2+} at a fast flow rate caused a more significant drop in the degree of hardening, and there were visible traces on the surface following dissolution. In conjunction with the results of the scanning electron microscopy experiments, which indicate that a fast flow rate affects the rate of soil erosion, the flow rate and the rate of karst soil erosion were positively correlated. A high flow rate of water causes the soil particles to erode more on the surface, resulting in stronger surface erosion.

An increase in flow rate will cause the amount of karst soil particles to erode, which will cause stronger fractures to occur [57,58].

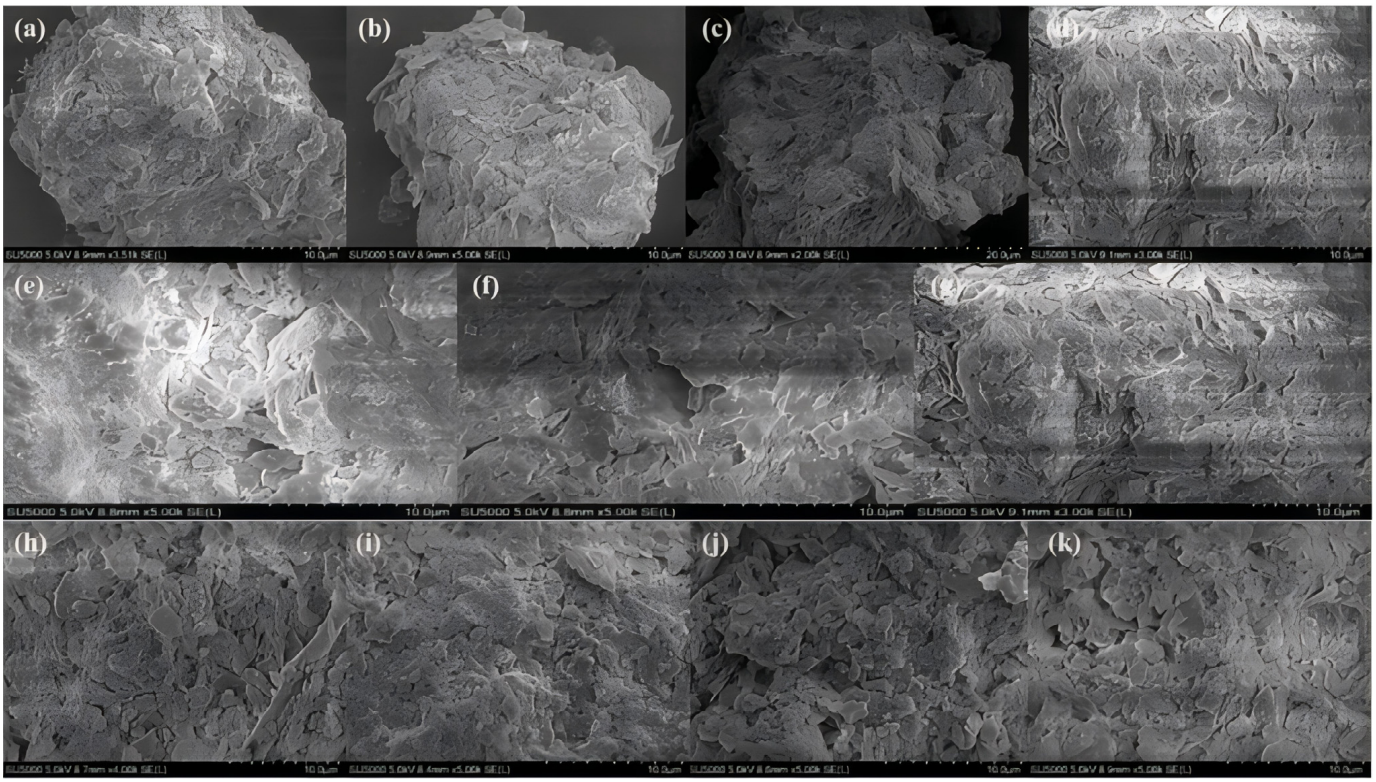

Figure 12. SEM images of soil: (**a**) karst soil before the reaction; (**b**) the ultra-pure water was injected at a flow rate of 0.41 mL/min; (**c**) 1 mg/L $ZnCl_2$ was administered at a flow rate of 0.41 mL/min; (**d**) 50 mg/L $ZnCl_2$ was administered at a flow rate of 0.41 mL/min; (**e**) the ultra-pure water was injected at a flow rate of 1.23 mL/min; (**f**) 1 mg/L $ZnCl_2$ was injected at a flow rate of 1.23 mL/min; (**g**) 50 mg/L $ZnCl_2$ was injected at a flow rate of 1.23 mL/min; (**h**) pre-reaction non-karst soil; (**i**) the ultra-pure water was injected at a flow rate of 1.23 mL/min; (**j**) 1 mg/L $ZnCl_2$ was injected at a flow rate of 1.23 mL/min; (**k**) 50 mg/L $ZnCl_2$ was injected at a flow rate of 1.23 mL/min; (**a**–**g**) the soil condition is karst soil; the soil condition of (**h**–**k**) is non-karst soil.

Figure 12h–k displays the non-karst soil morphology before and after the experiment. The shape of the non-karst soil changed somewhat after passing through the ultrapure water, 1 mg/L $ZnCl_2$, and 50 mg/L $ZnCl_2$. The particles became more compact. However, the difference was not really obvious. Prior to the reaction, the non-karst soil was heterogeneous, with smaller and larger particles than the limestone particles. In some locations, the particle shape was reasonably regular and smooth, whereas in others, the particles were bigger and partially angular. Pores of various diameters were visible between the particles. There was a slight shift that made the particles more compact, although it was barely detectable.

3.4.2. Limestone Morphological Characteristics

The morphology of the limestone under various reaction circumstances is shown in Figure 13, both before and after the reaction. The limestone samples were not uniform before the reaction, and there were visible pores of various sizes between the particles. Following the reaction between 1 mg/L and 50 mg/L of zinc chloride and ultrapure water, the limestone's morphology underwent a small alteration. Following the reaction with 50 mg/L $ZnCl_2$, the limestone in Figure 13d showed a faintly porous appearance, and tiny ruptures in the particles, but both the range and the number were minor. Furthermore, the limestone's surface exhibited fine, flaky crystal strips with hydrozincite

crystal characteristics [59,60]. This behavior is particularly obvious in Figure 13g,j, while Figure 13e–j displays the morphology of the limestone before and after the reaction at a high flow rate. The shape of the limestone changed more clearly in the high concentration and high flow rate environments, and, in addition to the surface hydrozincite adhesion, the amount of detrital material increased dramatically. The phenomenon of fine pinhole-like pores appearing on the surface of the limestone can be explained by the calcium carbonate breaking down on the surface, producing CO_2 and CaO, which cause internal loosening and flocculation [61]. Figure 13h–j depicts the shape of the limestone under non-karst soil conditions both before and after the reaction. The most noticeable change in morphology was the phase appearance of the limestone in the non-karst soil after 50 mg/L of Zn^{2+} was added at a high flow rate. All of the limestone surfaces had flakes, and the pores became larger, implying that the non-karst soil's specific surface area was smaller than that of the karst soil. The Zn^{2+} also adsorbed more on the limestone, placing significant pressure on the rock and generating a clear dissolving effect, which encouraged the interaction of the Zn^{2+} with the CO_3^{2-} and OH^- interactions, resulting in more hydrous zincite clinging to the limestone surface. Experiments using a scanning electron microscope show that the kind of soil and the soil's specific surface area both have a significant impact on the rate at which rocks dissolve.

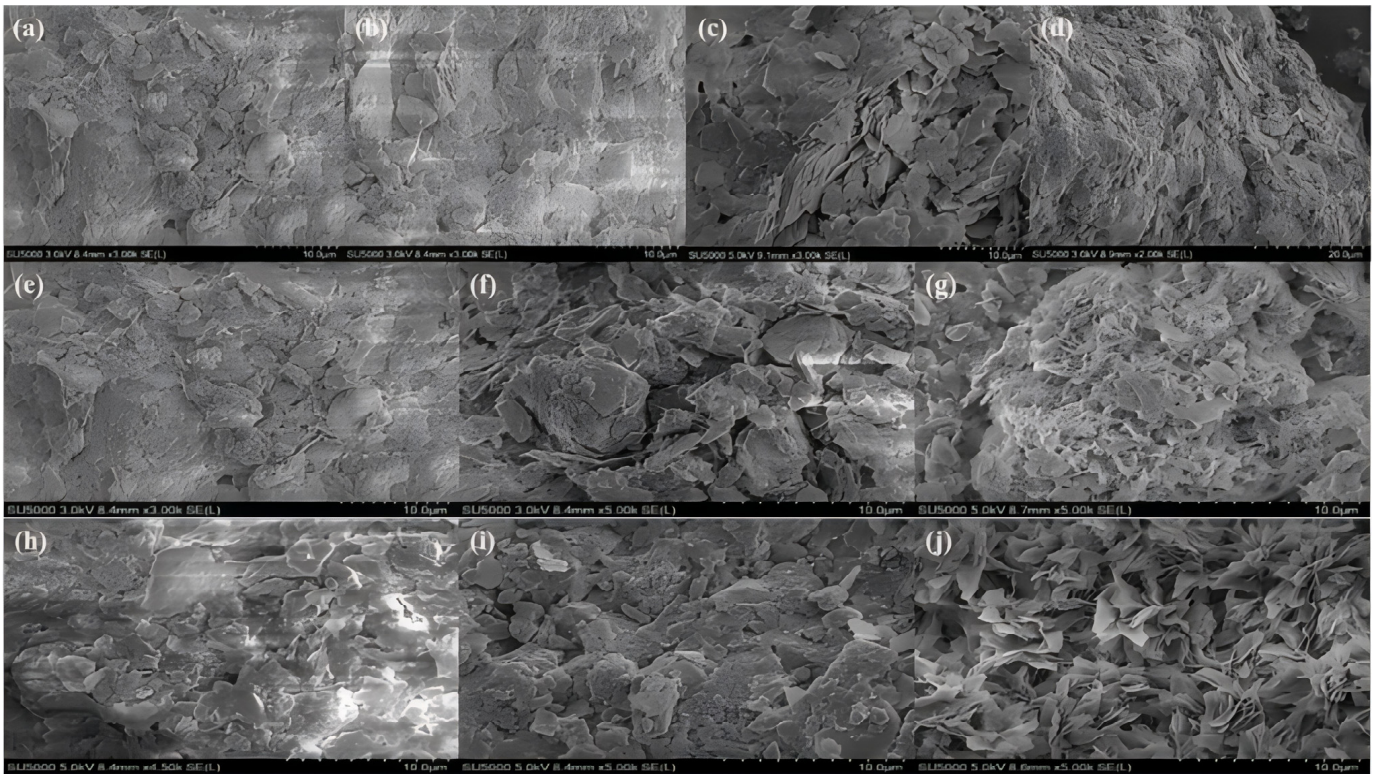

Figure 13. SEM images of limestone: (**a**) limestone before reaction; (**b**) ultrapure water passed at a flow rate of 0.41 mL/min; (**c**) 1 mg/L $ZnCl_2$ passed at a flow rate of 0.41 mL/min; (**d**) 50 mg/L $ZnCl_2$ passed at a flow rate of 0.41 mL/min; (**e**) the ultra-pure water was injected at a flow rate of 1.23 mL/min; (**f**) 1 mg/L $ZnCl_2$ at a flow rate of 1.23 mL/min; (**g**) 50 mg/L $ZnCl_2$ at a flow rate of 1.23 mL/min; (**h**) 1 mg/L $ZnCl_2$ at a flow rate of 1.23 mL/min to ultrapure water; (**i**) 1 mg/L $ZnCl_2$ at a flow rate of 1.23 mL/min; (**j**) 1 mg/L $ZnCl_2$ at a flow rate of 1.23 mL/min flow rate through 50 mg/L $ZnCl_2$; (**a**–**g**) soil conditions are karst soils; soil conditions in (**h**–**j**) are non-karst soils.

3.5. XPS Analysis of Limestone

The full spectrum of the binding energy on the limestone surface under various soil conditions to confirm the chemical composition of the new solid phase on the limestone surface was plotted (Figure 14). The energy spectrum peak at 284.80 eV was associated with

the calibration peak of C1s. With binding energies of 346.91 eV and 350.83 eV, respectively, the Ca2p spectrum can be split into two typical peaks, and Mg1s is responsible for the weak energy spectrum peak at 1303.83 eV. The reacted limestone, Zn2p, exhibited a double-peak type, with corresponding binding energies of 1021.8 eV and 1044.8 eV. For the Ca2p, Mg1s, $Zn2p_{1/2}$, and $Zn2p_{3/2}$, the narrow spectrum spectra are displayed to further ascertain the elemental morphology. The Ca2p's narrow spectrum shows that the changes in the concentration conditions had a significant impact on the chemical environment of the limestone surface (Figure 15a); changing the environmental conditions from top to bottom increased the binding energy by 0.98 eV, 0.19 eV, −0.35 eV, and −0.1 eV, respectively (Figure 15b). The chemical shift and peak were both dramatically altered. The low concentration of $ZnCl_2$ and soil participation enhanced the binding energy, although the peak value fell significantly. The peak value of the Mg^{2+} was higher in habitats with high concentrations, high flow rates, and no karst soil than it was in other settings. The peak value of the Mg^{2+} was larger than in other contexts, when the concentration and flow rate were high and the soil was non-karst; that is, the Mg^{2+} content was relatively high in these situations. When the full spectrum of the binding energy of the limestone surface was observed, the Zn exhibited more prominent spectral peaks, indicating that Zn^{2+} was transferred from the solution to the limestone's surface. When combined with the findings of earlier XPS studies of Zn compounds, the main Zn2p peak on the surface of the reacted limestone was a bimodal peak, and the main peaks of $Zn2p_{1/2}$ and $Zn2p_{3/2}$ [32] had narrow spectra, as shown in Figure 15c,d. The corresponding binding energies were 1045.33 eV, 1022.43 eV, 1045.42 eV, and 1021.77 eV. The appearance of the Zn-bearing solid phase on the limestone surface following the reaction in the Zn-bearing solution was further confirmed by comparing the XPS results for the limestone powder after the passage of 50 mg/L $ZnCl_2$ solution under various soil conditions. Characteristic peaks appeared in both samples near 1045 and 1022 eV, which corresponded to the $Zn2p_{1/2}$ and $Zn2p_{3/2}$ standard peak positions.

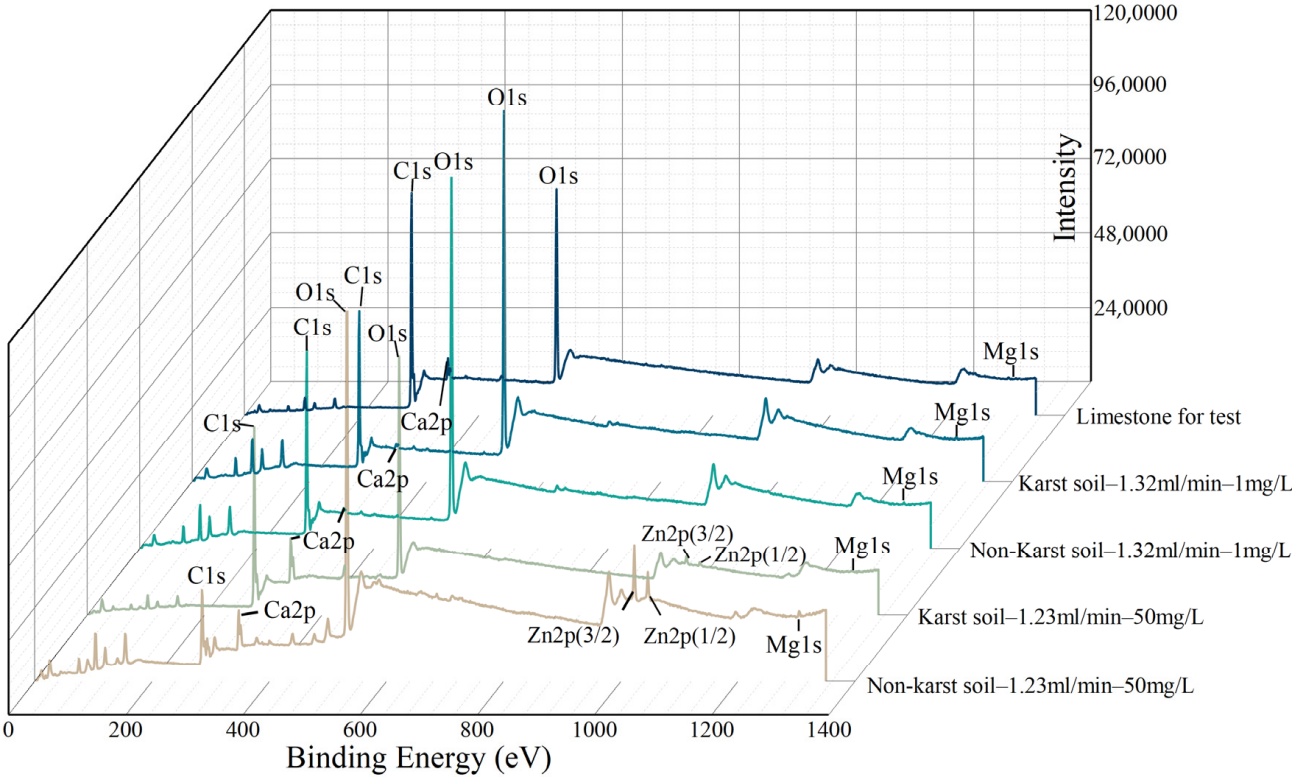

Figure 14. XPS full-spectrum scans of limestone.

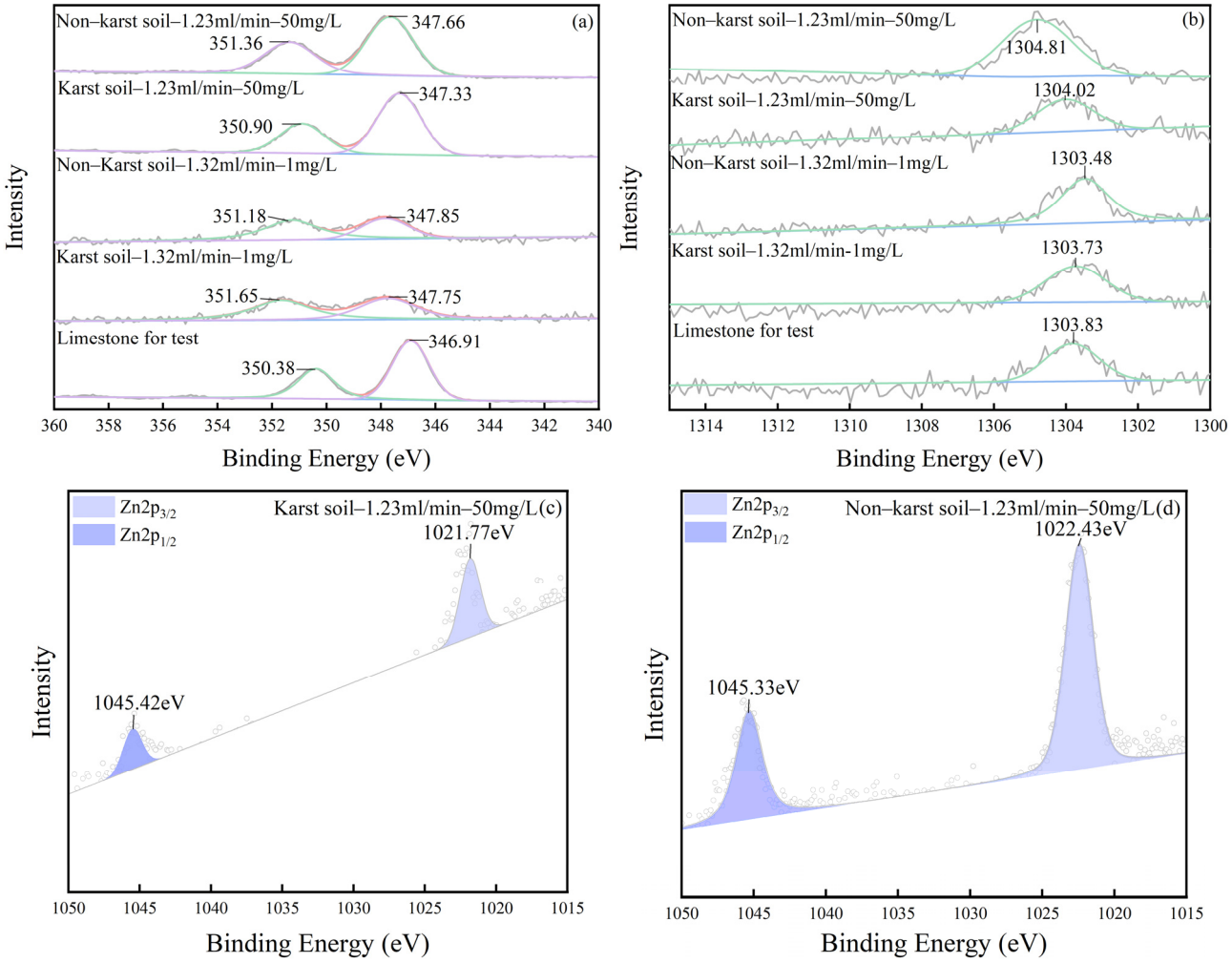

Figure 15. XPS narrow spectra of limestone: (**a**) Ca2p; (**b**) Mg1s; (**c**) Zn2p$_{3/2}$, (**d**) Zn2p$_{1/2}$.

4. Conclusions

Indoor dynamic experiments were utilized to investigate the interactions between Zn^{2+} and a soil-limestone system under different environmental conditions. During the dynamic adsorption process, an aqueous chemical analysis was combined with characterization analyses using XRD, FTIR, XPS, and SEM to produce the following primary conclusions:

(1) Two new Zn-containing solid phases formed in the soil-limestone system with the participation of the 50 mg/L $ZnCl_2$ solution; however, the phenomenon was not obvious in the 1 mg/L $ZnCl_2$ solution, and the Zn^{2+} acted mostly through ion exchange.

(2) Metal ion release in non-karst soils is quite different from that in karst soils due to the two types of soils' different mineral compositions, particle sizes, and surface areas. Non-karst soil has a smaller specific surface area than limestone, and more Zn^{2+} was adsorbed on the limestone in the non-karst soil-limestone combination. A bigger specific surface area might offer more adsorption sites.

(3) The $CaCO_3$ diffraction peaks on the surfaces of the soil and limestone particles diminished to various degrees, according to the XRD results; the non-karst soils' peaks in the 50 m/L $ZnCl_2$ solution showed the most pronounced declining tendency. The concentration, flow rate, and soil conditions all had an effect on the $CaCO_3$ on the limestone surface. A higher ion concentration promotes the dissolution of $CaCO_3$, but a higher flow rate mechanically damages rock samples' surfaces due to the erosive action of water flow. Additionally, the diffraction peaks of zinc hydrate and new solid-phase zinc carbonate are visible on the surfaces of soil and limestone. These peaks are more visible in situations with higher concentrations and flow rates, as

evidenced by the appearance of the characteristic Zn2p peaks in the XPS images and the thin strips of lamellar crystals on the surface of the limestone in the SEM images. The FT-IR test results show that the varied environmental conditions influenced the effect of the Zn^{2+} on the soil-limestone system. The effect on the soil-limestone system changed the distinct chemical environments in the water but did not change the functional groups of the soil-limestone.

In conclusion, the mechanism of Zn^{2+} adsorption and dissolution in soil-limestone systems is primarily expressed as adsorption and ion exchange at low concentrations, and ion exchange and surface precipitation at high concentrations of Zn^{2+} action. Regardless of the concentration, adding Zn^{2+} will promote the dissolution of $CaCO_3$ in the system, negatively impacting the carbon sink effect.

Author Contributions: Conceptualization, L.L. and Z.J.; methodology, Z.J.; validation, L.L., Z.J. and W.W.; formal analysis, Z.J.; investigation, B.W.; resources, L.L.; data curation, Z.J.; writing—original draft preparation, Z.J.; writing—review and editing, L.L.; visualization, W.W.; supervision, L.L.; project administration, L.L.; funding acquisition, L.L. All authors have read and agreed to the published version of the manuscript.

Funding: This research was funded by the National Natural Science Foundation of China—Regional Fund (42367027), the Guangxi Basic Ability Enhancement Project for Young and Middle-Aged Teachers (2020KY06034), and university-level scientific research projects, University of Science and Technology Scientific Research Initiation Fund (GLUTQD2013010).

Data Availability Statement: The original contributions presented in the study are included in the article, further inquiries can be directed to the corresponding author.

Acknowledgments: The authors would like to thank the School of Environmental Science and Engineering of Guilin University of Science and Technology and the Collaborative Innovation Centre for Water Pollution Control and Water Use Safety in Karst Areas for the laboratory instrumentation and equipment, as well as all the experts and editors for their valuable modifications of this paper in the course of reviewing the manuscript.

Conflicts of Interest: The authors declare that they have no known competing financial interests or personal relationships that could have appeared to influence the work reported in this paper.

References

1. Zhou, G. Recent progress in the study of heavy metal bioavailability in soil. *Wutan Yu Huatan* **2014**, *38*, 1097–1106.
2. Li, J.; Zhan, M.; Zhong, X.; Wang, X.; Ouyang, X.; Zhao, X. Distribution and accumulation of heavy metals in soil-crop systems from a typical carbonate rocks area in Guangxi. *Huanjing Kexue Xuebao* **2021**, *41*, 597–606.
3. He, L.; Wu, C.; Zeng, D.; Cheng, X.; Sun, B. Distribution of heavy metals and ecological risk of soils in the typical geological background region of southwest China. *Yankuang Ceshi* **2021**, *40*, 384–396.
4. Li, L.; Cao, J.; Huang, F.; Liang, Y.; Wang, P. Influence of lead-zinc minerals mining on river water environment and geological carbon sink. *Kuangye Yanjiu Yu Kaifa* **2013**, *33*, 89–92.
5. Wu, C.; Zhao, B.; Lu, Y.; Wang, J. Characteristics, risks and remediation of heavy metal polluted soils in typical karst regions: A Review. *Diqiu Yu Huanjing* **2023**, *51*, 549–563.
6. Li, R.; Gao, J.; Zhang, L.; Li, J.; Ji, H. Element geochemical characteristics of red weathering crust from dolomite, north Guizhou, China. *Zhongguo Yanrong* **2014**, *33*, 396–404.
7. Xiao, C.; Nie, H.; Liu, J.; Yuan, G.; Kang, Y.; Wang, A.; Song, B. Ecological and geological interaction model: The coupling of supergene geological processes and ecological characteristics. *Zhongguo Dizhi Diaocha* **2021**, *8*, 9–24.
8. Li, L.; Jiang, Z.; Wu, B.; Wei, D.; Wang, W. Influence of lead and zinc on geological carbon sink under oxygen-rich conditions. *Dixue Qianyuan* **2024**, 1–11. [CrossRef]
9. Huang, Q.; Qin, X.; Cheng, R.; Li, T.; Liu, P. Research progress of sulfuric acid rain participating in the dissolution of carbonate rocks. *Zhongguo Yanrong* **2019**, *38*, 149–156.
10. Liu, Z.; Macpherson, G.L.; Groves, C.; Martin, J.B.; Yuan, D.; Zeng, S. Large and active CO_2 uptake by coupled carbonate weathering. *Earth-Sci. Rev.* **2018**, *182*, 42–49. [CrossRef]
11. Wei, Y.; Li, W.; Wang, L. The significance of karst carbon sink for "carbon peak and carbon neutrality". *Zhongguo Kuangye* **2022**, *31*, 212–214.
12. Jiang, Z. Carbon cycle and ecological effects in eplkarst systems in southern China. *Disiji Yanjiu* **2000**, *20*, 316–324.

13. Zheng, X.; Lu, A.; Gao, X.; Zhao, J.; Zheng, D. Contamination of heavy metals in soil present situation and method. *Shengtai Huangjing Xuebao* **2002**, *1*, 79–84.
14. Zhu, A.; Chen, J.; Jiang, T.; Gao, L.; Chen, Y.; Zhong, J. Characteristics analysis of heavy metal pollution in soil alongside Hengshihe and Wengjiang river in Beijiang Basin. *Zhongguo Huanjing Kexue* **2015**, *35*, 506–515.
15. Li, J.; Yu, H.; Zeng, W.; Wu, X.; Yu, R. Research progress on plant growth promoting rhizobacteira and their role in phytoremediation of heavy metal-contaminated soil. *Shengming Kexue* **2017**, *29*, 434–442.
16. Liu, J.; Zhang, N.; Yu, H.; Zhang, J.; Li, F.; Yu, C.; Du, H. Effects of heavy metal pollution on microorganism and enzyme activity in paddy soil: A review. *Turang* **2021**, *53*, 1152–1159.
17. Hui, Y.; Pang, W.; Hu, M.; Shen, J. Analysis on analysis methods and prevention countermeasures of heavy metal pollution in soil. *Zhejiang Huagong* **2022**, *53*, 43–49.
18. Chen, S.; Wang, M.; Li, B.; Deng, H.; Lei, X.; Sun, X.; Wang, L. Current status of and discussion on farmland heavy metal pollution prevention in China. *Dixue Qianyuan* **2019**, *26*, 35–41.
19. Pu, J.; Jiang, Z.; Yuan, D.; Zhang, C. Some opinions on rock-weathering-related carbon sinks from the IPCC fifth assessment report. *Diqiu Kexue Jinzhan* **2015**, *30*, 1081–1090.
20. Wu, Q.; Guo, Y.; Xiao, Q.; Zhang, R.; Li, Y. Carbonates devote themselves to the target of "Double Carbon" silently. *Zhongguo Kuangye* **2022**, *31*, 215–216+243.
21. Qin, X.; Jiang, Z.; Zhang, L.; Huang, Q.; Liu, P. The difference of the weathering rate between carbonate rocks and silicate rocks and its effects on the atmospheric CO_2 consumption in the Pearl River Basin. Geological Bulletin of China. *Dizhi Tongbao* **2015**, *34*, 1749–1757.
22. Guan, T.; Li, L.; Liu, R.; Wu, B. Effect of lead ions on the dissolution of dolomite. *Guilin Ligong Daxue Xuebao* **2023**, *43*, 671–678.
23. Li, L.; Wu, B.; Guan, T.; Wang, W.; Wei, D. Divalent Lead in Aqueous Solution Changes the Surface Morphology of Dolomite and Inhibits Dissolution. *Water* **2022**, *14*, 2979. [CrossRef]
24. Li, L.; Cao, J.; Huang, F.; Liang, Y.; Wang, P. Relation models of Ca^{2+}, Mg^{2+} and HCO_3^- and analyses of carbon sinks influencing factors in the Chaotian River, Guilin. *Shuiwen Dizhi Gongcheng Dizhi* **2013**, *40*, 106–111.
25. Yi, L.; Xiang, R.; Wang, Z.; Lu, H.; Zhao, L. Infiltration coefficient of precipitation in karst peak-cluster depression area: A case study of Zhaidi karst underground river basin. *Zhongguo Yanrong* **2017**, *36*, 512–517.
26. Liu, P.; Xu, D.; Qin, X. Analysis of hydro-chemical characteristics and ion resource from Zhaidi underground river in Guilin. *Guilin Ligong Daxue Xuebao* **2016**, *36*, 234–241.
27. *DZ/T 0295-2016*; Specification of Land Quality Geochemical Assessment. Ministry of Land and Resources of the People's Republic of China, Geological Publishing House: Beijing, China, 2016.
28. Nazile, U. The significance of scanning electron microscopy (SEM) analysis on the microstructure of improved clay: An overview. *Open Geosci.* **2021**, *13*, 197–218.
29. Li, L.; Wang, W.; Jiang, Z.; Luo, A. Phosphate in Aqueous Solution Adsorbs on Limestone Surfaces and Promotes Dissolution. *Water* **2023**, *15*, 3230. [CrossRef]
30. Gong, Y.; Chen, X.; Wu, W. Application of fourier transform infrared (FTIR) spectroscopy in sample preparation: Material characterization and mechanism investigation. *Adv. Sample Prep.* **2024**, *11*, 100122. [CrossRef]
31. Powell, C.J.; Jablonski, A. Progress in quantitative surface analysis by X-ray photoelectron spectroscopy: Current status and perspectives. *J. Electron Spectrosc. Relat. Phenom.* **2009**, *178*, 331–346. [CrossRef]
32. Lavand, A.B.; Malghe, Y.S. Synthesis, characterization and visible light photocatalytic activity of carbon and iron modified ZnO. *J. King Saud. Univ. Sci.* **2018**, *30*, 65–74. [CrossRef]
33. Shi, Q.; Zhang, G.; Feng, Q.; Ou, L.; Lu, Y. Effect of the lattice ions on the calcite flotation in presence of Zn(II). *Miner. Eng.* **2013**, *40*, 24–29. [CrossRef]
34. Zhan, Q.; Qian, C. Microbial-induced remediation of Zn^{2+} pollution based on the capture and utilization of carbon dioxide. *Electron. J. Biotechnol.* **2016**, *19*, 29–32. [CrossRef]
35. Vega, F.A.; Covelo, E.F.; Andrade, M.L. The role of cation exchange in the sorption of cadmium, copper and lead by soils saturated with magnesium. *J. Hazard. Mater.* **2009**, *171*, 262–267. [CrossRef] [PubMed]
36. Zachara, J.M.; Cowan, C.E.; Resch, C.T. Sorption of divalent metals on calcite. *Geochim. Cosmochim. Acta* **1991**, *55*, 1549–1562. [CrossRef]
37. Zachara, J.; Kittrick, J.A.; Harsh, J. The mechanism of Zn^{2+} adsorption on calcite. *Geochim. Cosmochim. Acta* **1988**, *52*, 2281–2291. [CrossRef]
38. Aziz, H.A.; Adlan, M.N.; Ariffin, K.S. Heavy metals (Cd, Pb, Zn, Ni, Cu and Cr(III)) removal from water in Malaysia: Post treatment by high quality limestone. *Bioresour. Technol.* **2008**, *99*, 1578–1583. [PubMed]
39. Meng, J.Z.; Chen, S.L.; Wang, J.X.; Chen, Z.; Zhang, J.Y. Development and Application of Carbonate Dissolution Test Equipment under Thermal-Hydraulic-Chemical Coupling Condition. *Materials* **2022**, *15*, 7383. [CrossRef]
40. Elkhoury, J.E.; Ameli, P.; Detwiler, R.L. Dissolution and deformation in fractured carbonates caused by flow of CO_2 rich brine under reservoir conditions. *Int. J. Greenh. Gas Control* **2013**, *16*, S203–S215. [CrossRef]
41. Momber, A. Wear of rocks by water flow. *Int. J. Rock Mech. Min. Sci.* **2004**, *41*, 51–68. [CrossRef]
42. Yan, H.; Sedighi, M.; Jivkov, A. Modelling the effects of water chemistry and flowrate on clay erosion. *Eng. Geol.* **2021**, *294*, 106409. [CrossRef]

43. Shi, X.; Zhang, W.; Wang, H.; Jiao, X.; He, H. Modeling of water-rock interaction during the artificial recharge. *Jilin Daxue Xuebao Diqiu Kexueban* **2013**, *43*, 220–227+234.
44. Qin, Z.J.; Liu, F.; Lan, S.; Li, W.; Yin, H.; Zheng, L.R.; Zhang, Q. Effect of γ-manganite particle size on Zn^{2+} coordination environment during adsorption and desorption. *Appl. Clay Sci.* **2019**, *168*, 68–76. [CrossRef]
45. Wang, Y.; Wang, W.; Li, C.; Zhang, Y.; Xiao, F.; Zhao, X. Interference effect of exogenous organic matter on carbonate in light chernozem. *Jilin Nongye Daxue Xuebao* **2023**, *45*, 172–177.
46. Dong, W.; Li, Z.; Shen, L.; Liu, W.; Guo, Y.; Xu, H.; Yong, R. Study on the process of mass transfer and deterioration of limestone under dynamic dissolution of CO_2 solution. *Sci. Rep.* **2024**, *14*, 5278. [CrossRef] [PubMed]
47. Cherepanova, S.; Markovskaya, D.; Kozlova, E. Identification of a deleterious phase in photocatalyst based on $Cd_{1-x}Zn_xS/Zn(OH)_2$ by simulated XRD patterns. *Acta Crystallogr. Sect. B Struct. Sci.Cryst. Eng. Mat.* **2017**, *73*, 360–368. [CrossRef]
48. Liu, Y.; Ji, X.; Wang, Y.; Zhang, Y.; Zhang, Y.; Li, W.; Yuan, J.; Ma, D.; Sun, H.; Duan, J. A Stable Fe-Zn Modified Sludge-Derived Biochar for Diuron Removal: Kinetics, Isotherms, Mechanism, and Practical Research. *Molecules* **2023**, *28*, 2868. [CrossRef] [PubMed]
49. Li, M.; Kang, E.; Wang, J.; Yan, Z.; Zhang, K.; Hu, Z.Y.; Kang, X. Phosphorus accumulation poses less influence than soil physicochemical properties on organic phosphorus adsorption on ferrasol. *Geoderma* **2021**, *402*, 115324. [CrossRef]
50. Meyer-Jacob, C.; Vogel, H.; Boxberg, F.; Rosén, P.; Weber, M.E.; Bindler, R. Independent measurement of biogenic silica in sediments by FTIR spectroscopy and PLS regression. *J. Paleolimn.* **2014**, *52*, 245–255. [CrossRef]
51. Tkachenko, Y.; Niedzielski, P. FTIR as a method for qualitative assessment of solid samples in geochemical research: A review. *Molecules* **2022**, *27*, 8846. [CrossRef]
52. Chen, Y.; Furmann, A.; Mastalerz, M.; Schimmelmann, A. Quantitative analysis of shales by KBr-FTIR and micro-FTIR. *Fuel* **2014**, *116*, 538–549. [CrossRef]
53. Wang, Z.; Wu, H.; Xu, Y.; Shu, K.; Fang, S.; Xu, L. The effect of dissolved calcite species on the flotation of bastnaesite using sodium oleate. *Miner. Eng.* **2020**, *145*, 106095. [CrossRef]
54. Sdiri, A.; Higashi, T. Simultaneous removal of heavy metals from aqueous solution by natural limestones. *Appl. Water Sci.* **2013**, *3*, 29–39. [CrossRef]
55. Liu, R.; Liu, D.; Sun, R.; Wang, D.; Zhang, W.; Liu, Y.; Wen, S. Influence and mechanism of Zn^{2+} on fluorite/calcite in sodium hexametaphosphate flotation system. *Physicochem. Probl. Miner. Process.* **2022**, *58*, 151676. [CrossRef]
56. Liu, Q.; Xiang, W.; Zhang, W.; Cui, D. Experimental study of ionic soil stabilizer-improves expansive soil. *Yantu Lixue* **2009**, *30*, 2286–2290.
57. Keller, J.G.; Peijnenburg, W.; Werle, K.; Landsiedel, R.; Wohlleben, W. Understanding dissolution rates via continuous flow systems with physiologically relevant metal Ion saturation in lysosome. *Nanomaterials* **2020**, *10*, 311. [CrossRef]
58. Li, S.; Wang, Q.; Ma, L. Research of velocity and contaet area affecting the loess corrosion. *Shuili Yu Jianzhu Gongcheng Xuebao* **2008**, *3*, 103–104.
59. Liu, Z.; Teng, F. Understanding the Correlation of Crystal Atoms with Photochemistry Property: $Zn_5(OH)_6(CO_3)_2$ vs. $ZnCO_3$. *ChemistrySelect* **2018**, *3*, 8886–8894. [CrossRef]
60. Shahwan, T.; Zünbül, B.; Tunusoglu, Ö.; Eroglu, A.E. AAS, XRPD, SEM/EDS, and FTIR characterization of Zn^{2+} retention by calcite, calcite-kaolinite, and calcite-clinoptilolite minerals. *J. Colloid Interface Sci.* **2005**, *286*, 471–478. [CrossRef]
61. Galan, I.; Glasser, F.P.; Andrade, C. Calcium carbonate decomposition. *J. Therm. Anal. Calorim.* **2013**, *111*, 1197–1202. [CrossRef]